

Spectral Complex Autoencoder Pruning: A Fidelity-Guided Criterion for Extreme Structured Channel Compression

Wei Liu¹, Xing Deng¹, Haijian Shao¹, and Yingtao Jiang²

¹School of Computer, Jiangsu University of Science and Technology, Zhenjiang 212003, China

²Department of Electrical and Computer Engineering, University of Nevada, Las Vegas, 89115, USA

arXiv:2601.09352v1 [cs.CV] 14 Jan 2026

Abstract—We propose *Spectral Complex Autoencoder Pruning* (SCAP), a reconstruction-based criterion that measures functional redundancy at the level of individual output channels. For each convolutional layer, we construct a *complex interaction field* by pairing the full multi-channel input activation as the real part with a single output-channel activation (spatially aligned and broadcast across input channels) as the imaginary part. We transform this complex field to the frequency domain and train a low-capacity autoencoder to reconstruct normalized spectra. Channels whose spectra are reconstructed with high fidelity are interpreted as lying close to a low-dimensional manifold captured by the autoencoder and are therefore more compressible; conversely, channels with low fidelity are retained as they encode information that cannot be compactly represented by the learned manifold. This yields an importance score (optionally fused with the filter ℓ_1 norm) that supports simple threshold-based pruning and produces a structurally consistent pruned network. On VGG16 trained on CIFAR-10, at a fixed threshold of 0.6, we obtain 90.11% FLOP reduction and 96.30% parameter reduction with an absolute Top-1 accuracy drop of 1.67% from a 93.44% baseline after fine-tuning, demonstrating that spectral reconstruction fidelity of complex interaction fields is an effective proxy for channel-level redundancy under aggressive compression.

Index Terms—structured pruning, channel pruning, autoencoder, frequency domain, fidelity, CNN compression.

I. INTRODUCTION

MODERN convolutional neural networks (CNNs) remain a strong backbone for visual recognition on resource-constrained devices, yet their deployment is often bottlenecked by compute (FLOPs) and memory footprint (parameters). Structured *channel pruning*—removing entire convolutional output channels and rewiring subsequent layers accordingly—is particularly attractive because it yields practical speedups on standard hardware. However, achieving *extreme* compression (e.g., simultaneously reducing FLOPs and parameters by more than 90%) while keeping the post-fine-tuning accuracy drop within a small margin remains challenging. The core difficulty is not the mechanics of removing channels, but the design of a criterion that reliably identifies *functionally redundant* channels under distribution shift induced by pruning.

A large body of pruning work estimates channel importance from easily computed proxies such as filter magnitudes,

activation statistics, gradient/Taylor saliency, or combinations thereof. These proxies are computationally efficient and often work well at moderate pruning ratios, but they can become brittle at high compression: (i) magnitude-based pruning may discard low-norm channels that nevertheless capture rare but critical patterns; (ii) gradient-based criteria can be noisy and sensitive to the current mini-batch and optimization state; and (iii) layer-wise normalization and global thresholds can cause inconsistent pruning strength across layers, occasionally collapsing a crucial layer to too few channels and causing irreversible accuracy loss. More fundamentally, many proxies assess a channel in isolation, while redundancy is inherently *relational*: a channel is redundant only relative to what other channels already explain about the input-to-output transformation.

This paper proposes *Spectral Complex Autoencoder Pruning* (SCAP), a reconstruction-based criterion designed to measure redundancy at the level of a channel’s *input–output interaction*. Consider a convolutional layer with input activation $X \in \mathbb{R}^{B \times C_{\text{in}} \times H \times W}$ and output activation $Y \in \mathbb{R}^{B \times C_{\text{out}} \times H_1 \times W_1}$. For each output channel k , SCAP constructs a *complex interaction field*

$$Z_k = X + i \text{Broadcast}(\text{Resize}(Y_k)) \in \mathbb{C}^{B \times C_{\text{in}} \times H \times W},$$

where Y_k denotes the k -th output feature map, spatially aligned to (H, W) and broadcast across input channels. We then transform Z_k to the frequency domain and train a small-capacity autoencoder (one per layer) to reconstruct the normalized spectra. At scoring time, the autoencoder produces a reconstruction \hat{Z}_k and we compute a *fidelity* score as the cosine similarity between the vectorized original and reconstruction (real and imaginary parts concatenated), averaged over the batch. Intuitively, if a channel’s interaction field lies close to a low-dimensional manifold captured by the layer-wise autoencoder, then the channel expresses patterns already well explained by that manifold and is therefore more compressible; conversely, low fidelity indicates patterns that the low-capacity model cannot reproduce, suggesting higher novelty and importance.

This intuition can be stated more formally under a standard manifold-learning viewpoint. Let \mathcal{M}_ℓ denote the set of typical spectral interaction fields for layer ℓ induced by data and the current network. A sufficiently constrained autoencoder trained

to minimize reconstruction error over samples from \mathcal{M}_ℓ learns a mapping g_ℓ that approximates the identity on directions that are common and compressible under its bottleneck, while necessarily incurring larger error on directions that are rare or require higher intrinsic dimensionality than the bottleneck permits. Therefore, the reconstruction fidelity provides a principled *model-based* measure of compressibility: high fidelity implies that the interaction field is well represented by the learned low-dimensional structure, and pruning such channels is less likely to remove unique information *relative to the manifold captured by the autoencoder*. Importantly, SCAP does not claim that fidelity alone guarantees zero accuracy loss—pruning changes the network and the data-induced distribution of activations—but it provides a defensible, layer-local criterion grounded in compressibility rather than ad hoc statistics. In practice, we optionally fuse fidelity-derived importance with the filter ℓ_1 norm to guard against corner cases where a channel has high reconstructability yet remains salient due to amplitude.

Beyond the criterion itself, a practical obstacle is memory. Naïvely scoring all channels by expanding a batch to size $B \cdot C_{\text{out}}$ is prohibitive under limited GPU memory. SCAP is implemented with strict memory discipline: we process output channels sequentially (or in small groups), use gradient accumulation for autoencoder training, and explicitly release intermediate tensors (FFT outputs, reconstructions) to keep peak memory bounded. This allows training and scoring on commodity GPUs (e.g., 11 GB) without sacrificing the conceptual model. Our principal contributions are as follows:

- We introduce the complex interaction field representation that couples multi-channel inputs with per-channel outputs and enables relational redundancy analysis;
- we propose a frequency-domain, low-capacity autoencoder criterion and a fidelity-based importance score (with optional magnitude fusion) for threshold-based structured pruning.
- We provide a memory-efficient implementation via per-channel processing, gradient accumulation, and explicit tensor release.

II. RELATED WORK

A. Structured and channel pruning for CNN acceleration

Early pruning studies focused on removing individual weights using saliency measures derived from second-order approximations [1], [2]. Modern deep model compression revisited sparsification at scale and combined pruning with quantization and entropy coding [3], [4]. More recently, the community investigated the trainability and practicality of sparse subnetworks, including the lottery-ticket perspective and dynamic sparse training schemes [5]–[11], together with large-scale empirical assessments and surveys [12]–[14].

For deployment-oriented speedups, *structured* pruning removes entire channels/filters and preserves dense tensor shapes. Representative criteria include magnitude-based heuristics [15], sparsity regularization and re-scaling factors [16]–[18], gradient- or sensitivity-based importance [19],

[20], and discriminative pruning objectives [21]. A complementary thread formulates pruning as an optimization/automation problem, including reinforcement-learning or search based selection [22]–[24]. Many recent methods further improve stability by adopting “soft” or progressive deletion strategies [25]–[27]. These approaches are highly effective, but their scoring signals are often defined in the spatial domain and may not explicitly quantify *operator-level* redundancy between an input feature field and its induced output responses.

B. Reconstruction- and distillation-based pruning

Beyond pure saliency scoring, reconstruction-based criteria prune structures while explicitly preserving the layer-to-layer function. A classic example is using next-layer feature reconstruction to select channels/filters [28], [29]. Related ideas also appear in dynamic pruning/surgery pipelines [30] and in low-rank or factorized approximations that minimize reconstruction error under structural constraints [31]–[33]. Knowledge distillation provides another function-preserving signal by transferring “dark knowledge” or intermediate representations from a teacher to a compact student [34]–[36]. Autoencoders and denoising autoencoders are closely related tools for learning compact reconstructions and robust representations [37], [38]. Our method follows the reconstruction philosophy, but differs in that it measures per-filter reconstructability in the *spectral complex* space and turns it into a fidelity-driven importance signal.

C. Spectral-domain analysis and complex-valued representations

Using frequency-domain transforms to characterize neural representations has a long history, ranging from scattering-based invariants [39] to spectral pooling and spectral CNN analyses [40]. FFT-based implementations can also accelerate convolutions directly [41]. More recent work studies how Fourier features and periodic activations help neural networks model high-frequency functions [42], [43]. In parallel, complex-valued neural networks provide principled ways to model phase-sensitive signals and complex interactions [44], [45]. These perspectives motivate our design: SCAP constructs a complex interaction field, scores reconstructability in the frequency domain, and uses a fidelity-like criterion to quantify whether a filter’s effect is largely redundant.

D. Information-theoretic and geometric perspectives

Information-theoretic viewpoints, such as the information bottleneck principle and its variational formulations, offer a lens to understand redundancy and compression in learned representations [46], [47]. From the optimization side, information geometry and Fisher-curvature approximations (e.g., natural gradients and K-FAC) connect parameter sensitivity to the underlying model manifold [48], [49]. Meanwhile, representational similarity analysis (e.g., CCA variants) provides tools to quantify functional overlap between layers or models [50]–[52]. SCAP is aligned with these themes: rather than relying on a single heuristic, it uses a reconstruction-based, spectrum-aware fidelity score and optionally fuses it

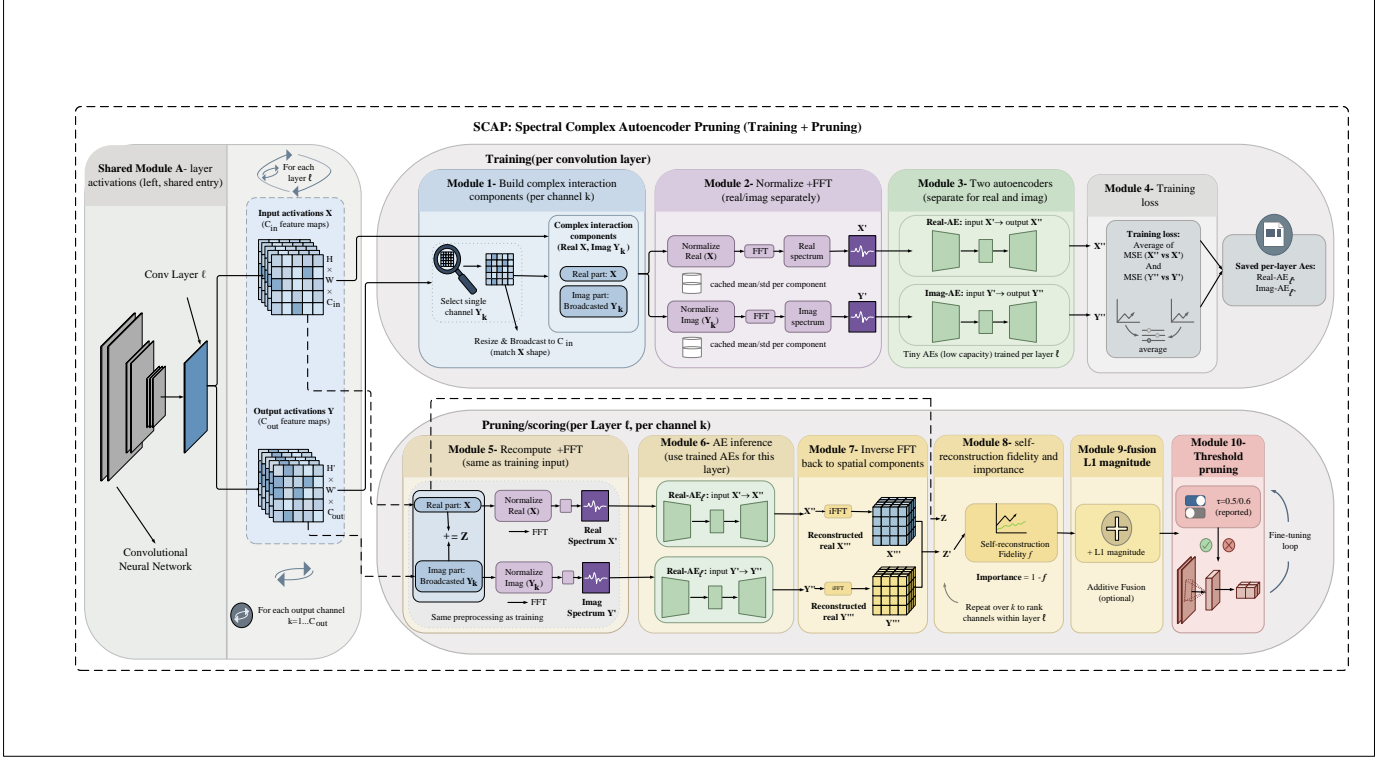


Fig. 1. Overview of SCAP (Spectral Complex Autoencoder Pruning). The method operates **layer-by-layer** and contains two stages. **Training:** for each convolutional layer ℓ and each output channel k , we build a channel-wise interaction descriptor by using the layer input activation as the real component and the resized-and-broadcast output feature map $Y_k^{(\ell)}$ as the imaginary component (broadcast to match the channel dimension of the input). After standardization and FFT, we obtain frequency-domain real/imag components, and train lightweight autoencoders *separately* for the real and imaginary parts using the average of the two MSE reconstruction losses. **Pruning:** given the trained per-layer autoencoders, we compute each channel's *self-reconstruction fidelity* by applying the same preprocessing, reconstructing in the frequency domain, transforming back with inverse FFT, and measuring cosine fidelity between the original and reconstructed (real, imag) interaction components. We define importance as $1 - \text{Fid}$ and optionally fuse it with a layer-normalized set- ℓ_1 magnitude term (additive fusion). Channels are kept or removed by a fixed threshold τ (we report only $\tau \in \{0.5, 0.6\}$), followed by standard fine-tuning of the structured pruned network.

with a normalized magnitude term, aiming to retain function while improving structural efficiency.

III. METHOD

We first give an overview of the proposed pipeline in Fig. 1. SCAP consists of two stages executed *layer-by-layer* over convolutional layers: (i) a **training stage** that learns lightweight spectral autoencoders for the real and imaginary components of a channel-wise interaction descriptor, and (ii) a **pruning stage** that evaluates each output channel by its self-reconstruction fidelity and removes redundant channels using a fixed threshold τ (reported at $\tau \in \{0.5, 0.6\}$), optionally fused with a layer-normalized set- ℓ_1 magnitude term. The rest of this section formalizes the setup and details each module in Fig. 1.

A. Problem setup

Consider a pretrained CNN f_θ with convolutional layers. For a convolutional layer ℓ , let the input activation be $X^{(\ell)} \in \mathbb{R}^{B \times C_{\text{in}} \times H \times W}$ and the output activation be $Y^{(\ell)} \in \mathbb{R}^{B \times C_{\text{out}} \times H_1 \times W_1}$. Our goal is *structured* pruning: we remove a subset of output channels (filters) and rewire subsequent layers accordingly, producing a smaller network \tilde{f}_θ with reduced

FLOPs and parameters while preserving accuracy after fine-tuning.

A central design choice is how to quantify channel redundancy. In this work, we assess redundancy by measuring how well a low-capacity model can reconstruct the *input–output interaction* associated with each output channel in the frequency domain. As illustrated in Fig. 1, we instantiate this idea by constructing a channel-wise complex interaction descriptor for each output channel and measuring its self-reconstruction fidelity under a low-capacity spectral reconstructor. In the following, we first formalize the descriptor construction, then describe the per-layer autoencoder training, and finally present the pruning rule and the optional set- ℓ_1 fusion.

B. Complex interaction field

For each output channel $k \in \{1, \dots, C_{\text{out}}\}$ of layer ℓ , we define a *complex interaction field*

$$Z_k^{(\ell)} = X^{(\ell)} + i \cdot \text{Broadcast}(\text{Resize}(Y_k^{(\ell)})) \in \mathbb{C}^{B \times C_{\text{in}} \times H \times W}, \quad (1)$$

where $Y_k^{(\ell)} \in \mathbb{R}^{B \times 1 \times H_1 \times W_1}$ is the k -th output feature map, $\text{Resize}(\cdot)$ aligns it to spatial size (H, W) (bilinear interpolation in our implementation), and $\text{Broadcast}(\cdot)$ replicates it across

the C_{in} input channels. Importantly, the real part uses the *full multi-channel* input activation $Z_k^{(\ell)}$.

a) *Why complex-valued coupling?*: Equation (1) couples the layer input and a specific output channel into one structured object. Since redundancy is defined relative to the input–output transformation, Z_k captures more relational information than statistics computed solely from weights or activations.

C. Spectral representation and normalization

We apply a 2D Fourier transform over spatial dimensions to obtain the spectral field:

$$\mathcal{F}(Z_k^{(\ell)}) = \text{FFT2}(Z_k^{(\ell)}) = F_k^{(\ell)} \in \mathbb{C}^{B \times C_{\text{in}} \times H \times W}. \quad (2)$$

We denote its real and imaginary parts by $F_k^{(\ell),R} = \Re(F_k^{(\ell)})$ and $F_k^{(\ell),I} = \Im(F_k^{(\ell)})$. Before reconstruction, we standardize each mini-batch in the frequency domain:

$$\begin{aligned} \tilde{F}^R &= \frac{F^R - \mu_R}{\sigma_R + \varepsilon}, & \mu_R &= \mu(F^R), \sigma_R &= \sigma(F^R), \\ \tilde{F}^I &= \frac{F^I - \mu_I}{\sigma_I + \varepsilon}, & \mu_I &= \mu(F^I), \sigma_I &= \sigma(F^I). \end{aligned} \quad (3)$$

Here $\mu(\cdot)$ and $\sigma(\cdot)$ denote the mean and standard deviation computed over all entries of the *current* mini-batch tensor (across b, c, h, w) for the real and imaginary parts separately. We cache $(\mu_R, \sigma_R, \mu_I, \sigma_I)$ to undo this standardization before the inverse FFT in Eq. (7), applied separately to the real and imaginary parts, where $\mu(\cdot)$ and $\sigma(\cdot)$ are the batch mean and standard deviation, and $\varepsilon > 0$ avoids division by zero.

D. Tiny spectral autoencoder

For each layer ℓ , we train a *layer-specific* low-capacity reconstructor g_{ϕ_ℓ} that maps $(\tilde{F}^R, \tilde{F}^I) \mapsto (\hat{F}^R, \hat{F}^I)$. To keep capacity intentionally limited (so that only common/compressible structure is reconstructed well), we adopt a tiny MLP applied *per channel* and shared across channels:

$$\begin{aligned} &\text{reshape } \tilde{F}^R \in \mathbb{R}^{B \times C_{\text{in}} \times H \times W} \\ &\mapsto U^R \in \mathbb{R}^{(B \cdot C_{\text{in}}) \times N}, \quad N = H \cdot W, \end{aligned}$$

and similarly for \tilde{F}^I . We then apply a shared MLP $h(\cdot)$ to each row:

$$\hat{U}^R = h(U^R), \quad \hat{U}^I = h(U^I),$$

and reshape back to $\hat{F}^R, \hat{F}^I \in \mathbb{R}^{B \times C_{\text{in}} \times H \times W}$. This design is *channel-adaptive*: it supports arbitrary C_{in} because channels are batched, and the parameter count depends primarily on $N = H \cdot W$ rather than C_{in} .

A concrete instantiation of h is:

$$h(u) = \text{Tanh}\left(W_2 \text{ReLU}(W_1 u)\right), \quad (4)$$

with $W_1 \in \mathbb{R}^{\frac{N}{4} \times N}$ and $W_2 \in \mathbb{R}^{N \times \frac{N}{4}}$.

a) *Training objective*.: For each layer ℓ , we train g_{ϕ_ℓ} using mean squared error in the normalized spectral domain:

$$\mathcal{L}_{\text{AE}}^{(\ell)} = \mathbb{E}_{k,b} \left[\|\hat{F}_k^{(\ell),R} - \tilde{F}_k^{(\ell),R}\|_2^2 + \|\hat{F}_k^{(\ell),I} - \tilde{F}_k^{(\ell),I}\|_2^2 \right]. \quad (5)$$

We implement this efficiently by iterating over output channels k (or small groups) and using gradient accumulation to emulate a larger batch under limited GPU memory.

E. Fidelity score and importance

After training, we freeze g_{ϕ_ℓ} and score each output channel by its reconstruction fidelity. For a mini-batch, we compute $(\mu_R, \sigma_R, \mu_I, \sigma_I)$ as in Eq. (3), feed the standardized spectra $(\tilde{F}^R, \tilde{F}^I)$ into g_{ϕ_ℓ} to obtain reconstructed standardized spectra (\hat{F}^R, \hat{F}^I) , and then undo the standardization:

$$\begin{aligned} \hat{F}^R &= (\sigma_R + \varepsilon) \hat{F}^R + \mu_R, \\ \hat{F}^I &= (\sigma_I + \varepsilon) \hat{F}^I + \mu_I, \quad \hat{F} = \hat{F}^R + i\hat{F}^I. \end{aligned} \quad (6)$$

We then invert the transform to obtain a reconstructed interaction field:

$$\hat{Z}_k^{(\ell)} = \text{iFFT2}(\hat{F}_k^{(\ell)}). \quad (7)$$

Let $\text{vec}(\cdot)$ flatten all tensor entries, and define the real-valued embedding

$$\begin{aligned} v_{k,b}^{(\ell)} &= \text{vec}([\Re(\hat{Z}_{k,b}^{(\ell)}), \Im(\hat{Z}_{k,b}^{(\ell)})]) \in \mathbb{R}^D, \\ \hat{v}_{k,b}^{(\ell)} &= \text{vec}([\Re(\hat{Z}_{k,b}^{(\ell)}), \Im(\hat{Z}_{k,b}^{(\ell)})]). \end{aligned}$$

We compute the per-sample cosine similarity and average across the batch:

$$\text{Fid}_k^{(\ell)} = \frac{1}{B} \sum_{b=1}^B \left| \frac{\langle v_{k,b}^{(\ell)}, \hat{v}_{k,b}^{(\ell)} \rangle}{\|v_{k,b}^{(\ell)}\|_2 \|\hat{v}_{k,b}^{(\ell)}\|_2} \right| \in [0, 1]. \quad (8)$$

a) *A useful identity (rigorous link to reconstruction error)*.: Define normalized vectors $u = v/\|v\|_2$ and $\hat{u} = \hat{v}/\|\hat{v}\|_2$. Let $F = |\langle u, \hat{u} \rangle|$. Then there exists $s \in \{+1, -1\}$ such that $\langle u, s\hat{u} \rangle = F$ and

$$\|u - s\hat{u}\|_2^2 = 2(1 - F). \quad (9)$$

Proof. Choose $s = \text{sign}(\langle u, \hat{u} \rangle)$. Since $\|u\|_2 = \|\hat{u}\|_2 = 1$, $\|u - s\hat{u}\|_2^2 = \|u\|_2^2 + \|\hat{u}\|_2^2 - 2\langle u, s\hat{u} \rangle = 2 - 2F = 2(1 - F)$.

□

Equation (9) shows that high fidelity is *equivalent* to small normalized reconstruction error up to a global sign. Therefore, $1 - \text{Fid}_k$ is a principled, scale-invariant measure of how far the reconstructed interaction is from the original in normalized ℓ_2 geometry.

b) *Importance score*.: We define the base importance as

$$I_{k,\text{fid}}^{(\ell)} = 1 - \text{Fid}_k^{(\ell)}. \quad (10)$$

Optionally, we fuse $I_{k,\text{fid}}$ with the filter ℓ_1 norm to guard against failure modes where a highly reconstructable channel nonetheless has large amplitude:

$$I_{k,11}^{(\ell)} = \frac{\|W_k^{(\ell)}\|_1}{\max_j \|W_j^{(\ell)}\|_1 + \varepsilon}, \quad I_k^{(\ell)} = \Psi(I_{k,\text{fid}}^{(\ell)}, I_{k,11}^{(\ell)}), \quad (11)$$

where $W_k^{(\ell)}$ denotes the k -th filter weights (flattened), and Ψ can be: (i) additive fusion, (ii) multiplicative fusion, or (iii) power-multiplicative fusion. In our experiments, we observed that the additive fusion consistently yields the best accuracy–compression trade-off and the most stable layer-wise pruning behavior; therefore, unless otherwise stated, we adopt additive fusion as the default choice in all reported results. We then map $\{I_k\}$ to $[0, 1]$ *within the layer* for thresholding.

F. Threshold-based structured pruning

Given a fixed threshold τ , we keep channels

$$\mathcal{K}_\ell = \{k : I_{k,\text{norm}}^{(\ell)} \geq \tau\}.$$

In practical applications, the value of τ is usually within a reasonable range (we found that setting τ to 0.5 and 0.6 can cover a typical range of trade-offs). We enforce a small safeguard to prevent a layer from collapsing: if $|\mathcal{K}_\ell| < K_{\min}(\ell)$, we keep the top- $K_{\min}(\ell)$ channels by $I_{k,\text{norm}}^{(\ell)}$. Notably, in all experiments reported in this paper, this safeguard is *never triggered*, indicating that the learned importance scores yield stable per-layer retention without requiring emergency constraints. After selecting \mathcal{K}_ℓ , we prune convolutional filters accordingly and propagate the channel selection to the next layer by removing the corresponding input channels. This yields a valid structured network that can be fine-tuned with standard training.

G. Memory-efficient implementation

A naïve implementation would score all (b, k) pairs by expanding tensors to size $B \cdot C_{\text{out}}$, which is prohibitive at high-resolution layers. We instead implement SCAP with strict memory discipline:

- **Per-output-channel processing:** construct and score Z_k for one output channel (or a small group) at a time rather than materializing all k simultaneously.
- **Gradient accumulation:** train the spectral autoencoder with micro-batches and accumulate gradients for n_{acc} steps before updating parameters, matching a larger effective batch size.
- **Explicit tensor release:** free FFT outputs and reconstructions immediately after each step (and clear CUDA cache when needed), keeping peak memory bounded.

This makes SCAP practical on limited GPUs (e.g., 11 GB) without changing the mathematical definition of fidelity or the pruning criterion.

a) *Discussion of scope.*: SCAP provides a compressibility-grounded, layer-local importance measure: channels whose interaction fields lie close to the low-capacity reconstructor's learned set achieve high fidelity and are treated as more redundant. This does *not* constitute a guarantee of zero accuracy loss under pruning, since pruning changes network dynamics and the activation distribution. Rather, SCAP furnishes a defensible and empirically effective proxy for redundancy, which we validate under aggressive compression in Section IV.

IV. EXPERIMENTS

A. Experimental settings

a) *Datasets and evaluation.*: We evaluate SCAP on **CIFAR-10** and **CIFAR-100** under the standard CIFAR protocol [53]. Both datasets contain 60K 32×32 RGB images, split into 50K training and 10K test images; CIFAR-10 has 10 classes and CIFAR-100 has 100 classes. We use standard data augmentation, including random cropping with padding and random horizontal flipping. All results are reported as **Top-1** test accuracy on the official test set, together with FLOPs and parameter reductions.

b) *Backbones and baseline checkpoints.*: We consider four widely used CNN backbones in structured pruning benchmarks: **VGG16** [54], **ResNet-56/ResNet-110** [55], and **DenseNet-40** [56]. For each backbone and dataset, we first train a baseline model and record its Top-1 accuracy, FLOPs, and parameter count as the reference checkpoint (Table I). All pruning results in this paper are measured as accuracy changes *relative to the corresponding baseline checkpoint* of the same model and dataset.

c) *Pretraining and fine-tuning protocol.*: All four models are pretrained for **200 epochs** using SGD with momentum 0.9, weight decay 5×10^{-4} , and batch size 256. The initial learning rate is set to 0.1 and decayed by a factor of 10 every 50 epochs. After pruning, we fine-tune the pruned networks for **100 epochs** using the same optimizer and batch size, with a reduced initial learning rate of 0.01 that is decayed by a factor of 10 every 30 epochs. Unless otherwise stated, these hyperparameters are kept fixed across architectures and datasets to ensure fair comparisons.

d) *Layer-wise spectral autoencoder training.*: SCAP trains one lightweight spectral autoencoder per convolutional layer. For each layer ℓ , we cache activations $(X^{(\ell)}, Y^{(\ell)})$ from a small pool of training images and construct a complex interaction field $Z_k^{(\ell)}$ for each output channel k (Eq. (1)). We compute its 2D FFT (Eq. (2)), apply per-batch spectral standardization (Eq. (3)), and optimize the reconstructor by minimizing the spectral MSE objective (Eq. (5)). The autoencoder is trained for **100 epochs** with learning rate 10^{-3} and weight decay 10^{-5} , using batch size 128.

e) *Memory-bounded implementation.*: To make both training and scoring feasible on a single commodity GPU, we adopt: (i) *per-output-channel* processing (iterating over k instead of materializing all channels at once), (ii) *gradient accumulation* to stabilize optimization under micro-batches, and (iii) explicit release of intermediate FFT and reconstruction tensors immediately after use.

f) *Primary operating points and scoring rule.*: Unless otherwise stated, we report SCAP at two fixed thresholds, $\tau \in \{0.5, 0.6\}$, on both CIFAR-10 and CIFAR-100. This choice is intentional: $\tau = 0.5$ represents a strong yet relatively safe compression regime, while $\tau = 0.6$ probes a more aggressive setting. For scoring, our default configuration uses the **additive fusion** in Eq. (11), $\Psi_{\text{add}}(I_{\text{fid}}, I_{11}) = \alpha I_{\text{fid}} + (1 - \alpha) I_{11}$. Here I_{11} is a **set- ℓ_1 magnitude** term normalized within each layer by $\max_j \|W_j^{(\ell)}\|_1$ (Eq. (11)), so the final importance is effectively a **sum of fidelity-based importance and set- ℓ_1 magnitude**. Alternative fusion rules (multiplicative and power-multiplicative) are analyzed in the Appendix (Exploratory experiments; Figs. 6–9), where we select the fusion behavior by jointly considering **compression ratios** and **Top-1 accuracy** trends.

g) *Implementation and hardware.*: All experiments are implemented in PyTorch and run on a single NVIDIA GeForce RTX 2080Ti GPU with 11GB memory, ensuring reproducible and efficient training/pruning across different backbone sizes.

TABLE I

THE MODEL'S TOP-1 BASELINE ACCURACY ON CIFAR-10/100. FLOPS ARE REPORTED AS MULTIPLY-ADD OPERATIONS (IN MILLIONS) AT CIFAR INPUT RESOLUTION; PARAMS ARE IN MILLIONS.

Dataset	Model	Top-1 Acc (%)	FLOPs (M)	Params (M)
CIFAR-10	VGGNet-16	93.44	314.57	14.99
	ResNet-56	93.66	130.02	0.88
	ResNet-110	92.63	259.49	1.75
	DenseNet-40	93.72	292.50	1.06
CIFAR-100	VGGNet-16	71.77	341.62	15.04
	ResNet-56	70.82	130.03	0.88
	ResNet-110	71.26	259.50	1.76
	DenseNet-40	72.95	292.54	1.10

TABLE II

THE EXPERIMENTAL RESULTS OF VGG-16 ON CIFAR-10/100.

Model	Dataset	Method	Baseline (%)	Pruned (%)	Top-1 acc ↓(%)	FR (%)	PR (%)
VGGNet-16	CIFAR-10	ℓ_1 -norm [15]	93.96	93.40	0.56	34.34	63.95
		SSS [18]	93.96	93.02	0.94	41.62	73.77
		GAL-0.05 [57]	93.96	92.03	1.93	39.60	77.60
		CP [29]	93.59	93.18	0.41	39.10	73.30
		Zhao et al. [58]	93.83	93.18	0.65	39.40	73.30
		GAL-0.1 [57]	93.96	90.73	3.23	45.20	82.20
		HRank [27]	93.96	92.34	1.62	65.30	82.10
		CSHE [59]	93.96	92.00	1.96	69.00	82.10
		Chen et al. [60]	93.91	93.17	0.74	52.30	45.70
		PCC [61]	94.59	94.12	0.47	66.19	84.41
	CIFAR-100	SCAP($\tau = 0.5$)	93.44	92.67	0.77	81.85	92.37
		SCAP($\tau = 0.6$)	93.44	91.77	1.67	90.11	96.30
VGGNet-16	CIFAR-100	Zhao et al. [58]	73.54	73.33	0.21	18.40	38.10
		FPGM [26]	73.51	72.26	1.25	51.01	51.01
		SFP [62]	73.51	71.74	1.77	41.75	39.34
		HRank [27]	73.51	72.43	1.08	41.23	55.93
		COP v1 [63]	73.51	72.63	0.88	40.31	65.19
		Li et al. [64]	72.53	72.44	0.09	39.55	65.94
		PCC [61]	74.02	73.94	0.08	28.57	27.67
		SCAP($\tau = 0.5$)	71.77	68.26	3.51	79.62	84.65
		SCAP($\tau = 0.6$)	71.77	62.79	8.98	90.70	92.37

B. Metrics and reporting

We report FLOP reduction (FR) and parameter reduction (PR) relative to the baseline checkpoint:

$$PR = 100 \left(1 - \frac{P(\tilde{f})}{P(f)} \right) \%, \quad FR = 100 \left(1 - \frac{F(\tilde{f})}{F(f)} \right) \%$$

Accuracy is Top-1 on the test set, and the absolute accuracy drop is defined as $\Delta \text{Acc} = \text{Acc}(f) - \text{Acc}(\tilde{f})$.

C. Results and method comparison

VGG-16. Table II summarizes the results on CIFAR-10 and CIFAR-100. SCAP achieves substantial parameter and FLOPs reduction while maintaining competitive accuracy. On CIFAR-10, SCAP($\tau = 0.5$) compresses VGG-16 by **81.85% FR** and **92.37% PR**, with only a **0.77% Top-1 accuracy drop** compared with the baseline (93.44% vs. 92.67%). When pruning more aggressively at $\tau = 0.6$, the accuracy gap slightly increases to 1.67%, but the model reaches **90.11% FLOPs reduction** and **96.3% parameter reduction**. On CIFAR-100, SCAP maintains consistent behavior: with $\tau = 0.5$, Top-1 accuracy drops only 3.51% while achieving **79.62% FR** and **84.65% PR**; for $\tau = 0.6$, compression reaches over **90.70%**

FLOPs reduction with 8.98% accuracy degradation. These results demonstrate that spectral-based importance provides robust redundancy detection even under strong pruning.

ResNet. Table III reports results on both datasets. Compared with traditional magnitude-based or gradient-based methods (e.g., ℓ_1 -norm, FPGM, HRank), SCAP exhibits a better trade-off between accuracy and compression. On CIFAR-10, SCAP($\tau = 0.5$) achieves **72.41% FLOPs** and **71.36% parameter reduction** with a moderate 2.08% accuracy drop; at $\tau = 0.6$, pruning becomes more aggressive (**83.80% FLOPs** and **84.66% PR**) with a 3.76% loss. On CIFAR-100, the method generalizes well: the $\tau = 0.5$ setting removes nearly **69.27% of FLOPs** while retaining competitive performance, and $\tau = 0.6$ pushes the compression further to **82.06% FLOPs reduction** and **87.12% PR**, at the cost of a 13.2% drop in accuracy. Overall, SCAP demonstrates high pruning capacity for residual networks without requiring iterative fine-grained optimization. For the deeper ResNet-110 backbone (Table IV), SCAP effectively balances accuracy retention and compression across both CIFAR-10 and CIFAR-100. On CIFAR-10, SCAP($\tau = 0.5$) yields a **85.13% FLOPs reduction** and **82.67% PR** with a small 1.64% accuracy drop. When increasing to $\tau = 0.6$, the pruning rate rises to **89.39% FLOPs**

TABLE III
THE EXPERIMENTAL RESULTS OF RESNET-56 ON CIFAR-10/100.

Model	Dataset	Method	Baseline (%)	Pruned (%)	Top-1 acc ↓(%)	FR (%)	PR (%)
ResNet-56	CIFAR-10	ℓ_1 -norm [15]	93.04	93.06	-0.02	27.60	13.70
		NISP [20]	93.04	93.01	0.03	43.61	42.60
		GAL-0.6 [57]	93.26	93.38	-0.12	37.60	11.80
		HRank [27]	93.26	93.52	-0.26	29.30	16.80
		CHIP [65]	93.26	94.16	-0.90	47.40	42.80
		DTP [66]	93.36	92.46	0.90	72.10	—
		DepGraph [67]	93.53	93.77	-0.24	52.40	—
		Li et al. [67]	92.60	92.42	0.18	49.90	44.00
		CCM [68]	93.75	92.74	1.01	69.90	70.30
		CP [29]	93.26	90.80	2.46	50.60	—
		FTWT _J [69]	93.66	92.28	1.38	54.00	—
		FPGM [26]	93.59	93.49	0.10	52.60	50.60
		FPRG [70]	93.45	92.61	0.84	57.10	33.60
		PCC [61]	94.48	93.13	1.35	61.64	65.06
		SCAP($\tau = 0.5$)	93.66	91.58	2.08	72.41	71.36
		SCAP($\tau = 0.6$)	93.66	89.90	3.76	83.80	84.66
	CIFAR-100	ℓ_1 -norm [15]	70.83	69.10	1.73	47.02	17.50
		Li et al. [64]	70.83	69.99	0.84	47.02	17.50
		FPRG [70]	70.83	68.73	2.10	60.32	33.01
		PCC [61]	71.45	65.43	6.02	72.20	73.97
		SCAP($\tau = 0.5$)	70.82	65.42	5.40	69.27	74.43
		SCAP($\tau = 0.6$)	70.82	57.61	13.21	82.06	87.12

and **88.52% PR** with a 2.85% degradation. On CIFAR-100, similar trends hold: at $\tau = 0.5$, SCAP compresses the model by **77.05% FLOPs** and **74.84% PR** with a 4.80% drop, and under $\tau = 0.6$, achieves **84.38% FLOPs** and **84.36% PR** with 8.10% degradation. These results confirm that SCAP scales efficiently to deeper networks and preserves accuracy more effectively than FPGM or PCC under comparable compression ratios.

DenseNet-40. Table V presents results on DenseNet-40, where dense connectivity introduces inter-layer feature reuse and makes redundancy estimation more challenging. On CIFAR-10, SCAP($\tau = 0.5$) achieves a competitive **75.92% FLOPs** and **77.87% parameter reduction**, losing only 1.19% Top-1 accuracy. Under $\tau = 0.6$, accuracy drops by 2.21%, but compression further increases to **84.10% FLOPs** and **86.46% PR**. For CIFAR-100, SCAP($\tau = 0.5$) achieves **74.77% FLOPs** and **73.66% PR** with a 4.76% loss, while the $\tau = 0.6$ setting pushes the compression to **83.96% FLOPs** and **83.70% PR** with a corresponding 8.41% degradation. These results validate that SCAP remains effective even in architectures with strong feature reuse, outperforming prior pruning schemes such as HRank and DCT in both accuracy preservation and compression efficiency.

D. Ablation study

a) *What is ablated.*: In the main pipeline, SCAP computes the channel importance by an **additive fusion** of (i) the fidelity-derived importance I_{fid} and (ii) a **set- ℓ_1** magnitude term I_{11} (layer-wise normalized), i.e., the final importance explicitly **adds** the ℓ_1 component. Therefore, a proper ablation must remove the ℓ_1 term to verify whether the gain comes from the proposed fidelity signal alone or from the fusion.

b) *Compared variants.*: We evaluate two variants under the same pruning and fine-tuning protocol:

- **11-none**: importance uses **only** the fidelity term (I_{fid}), i.e., no ℓ_1 magnitude is used;

- **SCAP**: importance uses the **additive fusion** of fidelity and set- ℓ_1 magnitude ($I_{\text{fid}} + I_{11}$ with the same normalization and weights as in the main setting).

c) *Main-paper setting ($\tau = 0.5$ on CIFAR-100).*: The ablation results reported in the **main paper** (Figs. 2–3) are conducted on **CIFAR-100** at a fixed threshold $\tau = 0.5$. Figure 2 shows the fine-tuning trajectories across four backbones. Overall, **SCAP (with set- ℓ_1 addition)** exhibits more stable recovery and typically reaches higher final accuracy than **11-none**, indicating that the ℓ_1 magnitude provides a complementary regularizing cue that helps avoid pruning channels that are small in magnitude yet still functionally useful.

Figure 3 summarizes the final outcomes by jointly comparing **Top-1 accuracy** and **compression** (FR/PR). The key takeaway is that the default additive fusion in SCAP provides a better accuracy–compression trade-off than using the fidelity term alone under the same threshold.

d) *More aggressive setting ($\tau = 0.6$).*: We further provide the corresponding ablation at the more aggressive threshold $\tau = 0.6$ in the Appendix (Additional experiments; Figs. 4–5), where the trade-off becomes sharper.

V. CONCLUSION AND LIMITATIONS

We presented *Spectral Complex Autoencoder Pruning* (SCAP), a structured channel pruning framework designed for the extreme compression regime where both FLOP and parameter reductions exceed 90%. SCAP departs from proxy-based importance scores by explicitly modeling channel redundancy through *reconstructability* of an input–output interaction descriptor. For each convolutional layer, we construct a complex interaction field that couples the full multi-channel input activation with a per-channel output activation, transform it to the frequency domain, and train a deliberately low-capacity reconstructor. Channels that achieve high reconstruction fidelity are interpreted as lying close to a compressible manifold captured by the reconstructor and are therefore more redundant;

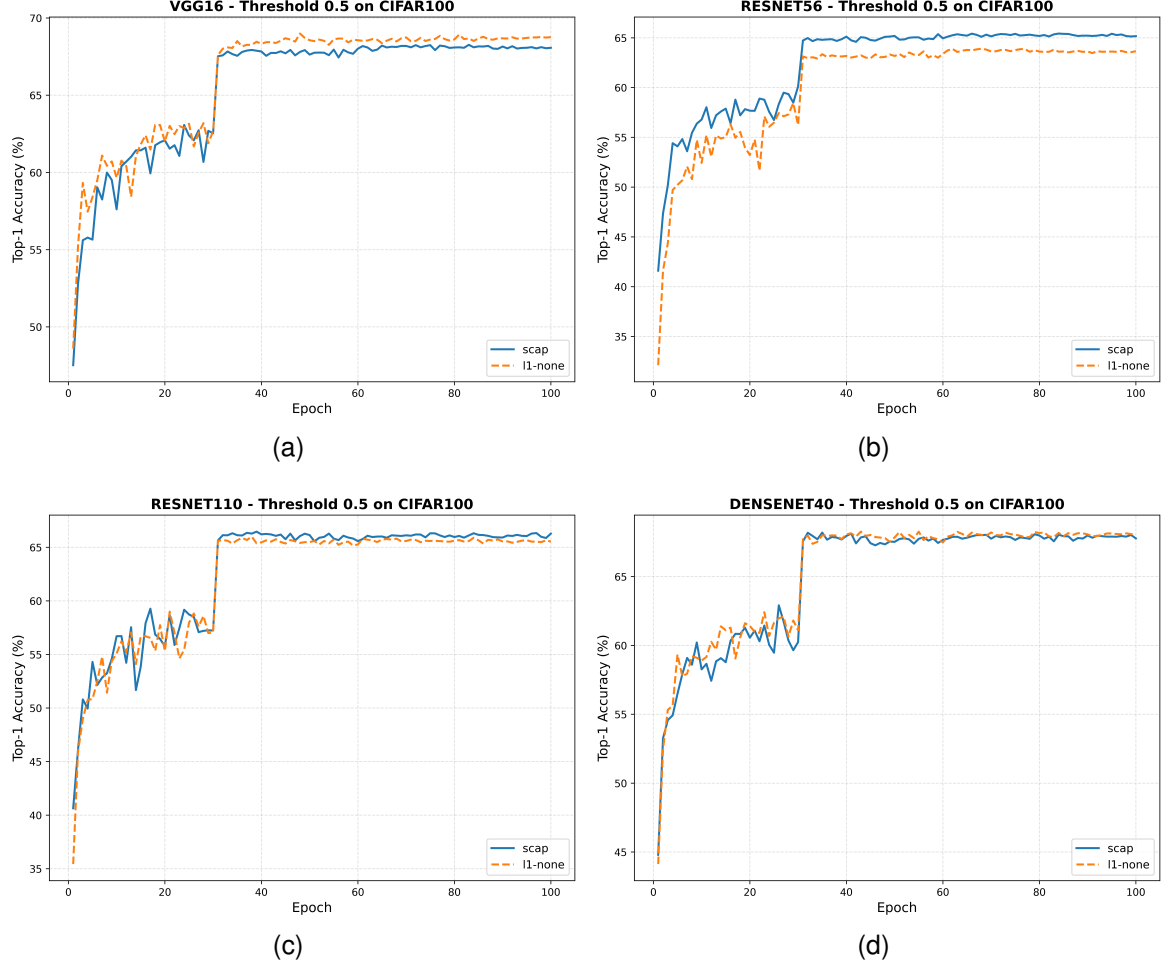


Fig. 2. Ablation at threshold $\tau = 0.5$ on CIFAR-100. **l1-none** denotes fidelity-only importance (removing the ℓ_1 magnitude term), while **SCAP** denotes the default additive fusion (fidelity + set- ℓ_1). We report Top-1 accuracy during fine-tuning for different backbones.

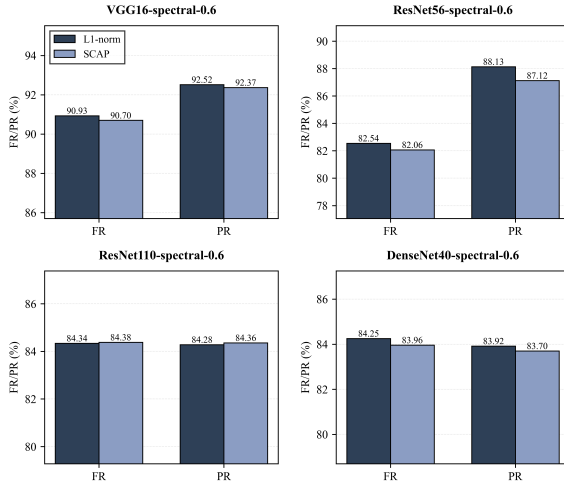


Fig. 3. Compression comparison (FR/PR) for the ablation at $\tau = 0.5$ on CIFAR-100. **l1-none** removes the ℓ_1 magnitude term; **SCAP** uses the default additive fusion (fidelity + set- ℓ_1).

channels with low fidelity are retained. We further established a rigorous link between fidelity and normalized reconstruction

error and provided a perturbation-style justification under a stability assumption, yielding a logically complete rationale for using $1 - \text{Fid}$ as an importance signal.

The empirical performance of SCAP suggests a coherent view that connects *compressibility* to an information-geometric notion of redundancy. In particular, spectral reconstruction fidelity can be interpreted as a proxy for how “regular” or “flat” a channel-specific interaction descriptor is with respect to the data-induced structure of layer activations: channels whose complex interaction fields concentrate around a low-dimensional, smoothly varying set tend to be reconstructed well by a low-capacity spectral autoencoder and are thus more likely to be redundant, whereas channels associated with more irregular, high-curvature variations are harder to reconstruct and are preferentially preserved. This geometric perspective helps unify many heuristic pruning signals under a single explanation: they often succeed insofar as they correlate with the ease of representing a channel on the dominant low-dimensional structure of the activation manifold.

a) Limitations.: SCAP provides a principled *layer-local* redundancy measure, but it does not constitute a global guarantee of accuracy preservation. Pruning changes network dynamics and the activation distribution, which necessitates fine-

TABLE IV
THE EXPERIMENTAL RESULTS OF RESNET-110 ON CIFAR-10/100

Model	Dataset	Method	Baseline (%)	Pruned (%)	Top-1 acc ↓(%)	FR (%)	PR (%)
ResNet-110	CIFAR-10	l_1 -norm [15]	93.53	93.30	0.23	38.70	32.40
		NISP [20]	93.50	93.32	0.18	43.78	43.25
		HRank [27]	93.50	94.23	-0.73	41.20	39.40
		CHIP [65]	93.50	94.44	-0.94	52.10	48.30
		GAL-0.5 [57]	93.50	92.74	0.76	48.50	44.80
		FPGM [26]	93.68	93.74	-0.16	52.30	—
		CCM [68]	94.14	93.80	0.34	69.40	68.40
		CPRNC [71]	93.50	94.16	-0.66	52.60	52.60
		FPRG [70]	93.94	92.27	1.67	62.70	32.10
		PCC [61]	94.90	92.95	1.95	77.47	78.77
	CIFAR-100	SCAP($\tau = 0.5$)	92.63	90.99	1.64	85.13	82.67
		SCAP($\tau = 0.6$)	92.63	89.78	2.85	89.39	88.52
ResNet-110	CIFAR-100	l_1 -norm [15]	70.95	69.88	1.07	52.42	20.72
		Li et al. [64]	70.95	70.27	0.68	52.42	20.72
		FPRG [70]	70.95	69.00	1.95	63.08	46.78
		PCC [61]	73.69	68.02	5.67	74.63	75.72
		SCAP($\tau = 0.5$)	71.26	66.46	4.80	77.05	74.84
		SCAP($\tau = 0.6$)	71.26	63.16	8.10	84.38	84.36

TABLE V
THE EXPERIMENTAL RESULTS OF DENSENET-40 ON CIFAR-10/100.

Model	Dataset	Method	Baseline (%)	Pruned (%)	Top-1 acc ↓(%)	FR (%)	PR (%)
DenseNet-40	CIFAR-10	GAL-0.01 [57]	94.81	94.29	0.52	35.13	35.58
		Li et al. [64]	94.19	93.00	1.19	43.09	24.03
		Zhao et al. [58]	94.11	93.16	0.95	44.78	59.67
		HRank [27]	94.81	93.68	1.13	60.94	53.85
		DCT [72]	94.81	94.32	0.49	38.50	40.40
		Chen et al. [60]	94.22	93.56	0.66	44.40	60.08
	CIFAR-100	Ous($t=0.5$)	93.72	92.53	1.19	75.92	77.87
		Ous($t=0.6$)	93.72	91.51	2.21	84.10	86.46
		Zhao et al. [58]	74.64	72.19	2.45	22.67	37.73
		Li et al. [64]	72.85	72.07	0.78	41.87	18.22
		l_1 -norm [15]	72.85	71.89	0.96	41.87	18.22
		Ous($t=0.5$)	72.95	68.19	4.76	74.77	73.66
		Ous($t=0.6$)	72.95	64.54	8.41	83.96	83.70

tuning. Moreover, the descriptor construction (broadcasting a single output map across input channels) is a specific design choice that emphasizes the relation between the layer input and a given output channel; alternative couplings may further improve sensitivity for certain architectures. Finally, as with any threshold-based method, stable per-layer normalization and safeguards against layer collapse remain important to avoid pathological decisions under extreme compression.

b) Outlook.: Several extensions are promising. First, SCAP can be generalized beyond CNNs by defining appropriate complex interaction fields for other operators (e.g., attention heads or MLP blocks in transformers) and reconstructing them in a frequency-like domain (e.g., token-frequency or graph spectral domains). Second, replacing the deterministic reconstructor with a probabilistic model (e.g., a variational spectral reconstructor) could provide uncertainty-aware importance scores and formalize redundancy via information-theoretic quantities. Third, the stability analysis in Section VI suggests a route to adaptive, layer-wise thresholds driven by bounded output perturbation rather than fixed τ , potentially enabling tighter control over accuracy under a prescribed compression budget. We believe these directions can further unify structured pruning with geometric and compressibility principles and lead to robust, deployment-ready model reduction methods.

REFERENCES

- [1] Y. LeCun, J. S. Denker, and S. A. Solla, “Optimal brain damage,” in *Advances in Neural Information Processing Systems (NeurIPS)*, 1990.
- [2] B. Hassibi and D. G. Stork, “Second order derivatives for network pruning: Optimal brain surgeon,” in *Advances in Neural Information Processing Systems (NeurIPS)*, 1993.
- [3] S. Han, J. Pool, J. Tran, and W. Dally, “Learning both weights and connections for efficient neural network,” in *Advances in Neural Information Processing Systems (NeurIPS)*, 2015, arXiv:1506.02626.
- [4] S. Han, H. Mao, and W. J. Dally, “Deep compression: Compressing deep neural networks with pruning, trained quantization and huffman coding,” in *International Conference on Learning Representations (ICLR)*, 2016, arXiv:1510.00149.
- [5] J. Frankle and M. Carbin, “The lottery ticket hypothesis: Finding sparse, trainable neural networks,” in *International Conference on Learning Representations (ICLR)*, 2019, arXiv:1803.03635.
- [6] T. Gale, E. Elsen, and S. Hooker, “The state of sparsity in deep neural networks,” *arXiv preprint arXiv:1902.09574*, 2019.
- [7] U. Evci, T. Gale, J. Menick, P. S. Castro, and E. Elsen, “Rigging the lottery: Making all tickets winners,” in *International Conference on Machine Learning (ICML)*, 2020, arXiv:1911.11134.
- [8] H. Tanaka, D. Kunin, D. L. K. Yamins, and S. Ganguli, “Synflow: Synaptic flow for neural network pruning,” in *International Conference on Learning Representations (ICLR)*, 2020, arXiv:2006.05467.
- [9] N. Lee, T. Ajanthan, and P. H. S. Torr, “Snip: Single-shot network pruning based on connection sensitivity,” in *International Conference on Learning Representations (ICLR)*, 2019, arXiv:1810.02340.
- [10] C. Wang, G. Zhang, R. Grosse *et al.*, “Picking winning tickets before training by preserving gradient flow,” in *International Conference on Learning Representations (ICLR)*, 2020, arXiv:2002.07376.
- [11] D. C. Mocanu, E. Mocanu, P. Stone, P. H. Nguyen, M. Gibescu, and A. Liotta, “Sparse evolutionary training: A scalable alternative to training

dense neural networks,” *Nature Communications*, vol. 9, no. 1, pp. 1–12, 2018, arXiv:1707.04780.

[12] D. Blalock, J. J. G. Ortiz, J. Frankle, and J. Guttag, “What is the state of neural network pruning?” *Proceedings of Machine Learning and Systems (MLSys)*, 2020, arXiv:2003.03033.

[13] Y. Cheng, D. Wang, P. Zhou, and T. Zhang, “A survey of model compression and acceleration for deep neural networks,” *arXiv preprint arXiv:1710.09282*, 2017.

[14] Y. Li *et al.*, “Structured pruning: A comprehensive survey,” *arXiv preprint arXiv:2303.00566*, 2023.

[15] D. Filters’Importance, “Pruning filters for efficient convnets,” *arXiv preprint arXiv:1608.08710*, 2016.

[16] W. Wen, C. Wu, Y. Wang, Y. Chen, and H. Li, “Learning structured sparsity in deep neural networks,” in *Advances in Neural Information Processing Systems (NeurIPS)*, 2016, arXiv:1608.03665.

[17] Z. Liu, J. Li, Z. Shen, G. Huang, S. Yan, and C. Zhang, “Learning efficient convolutional networks through network slimming,” in *IEEE International Conference on Computer Vision (ICCV)*, 2017.

[18] Z. Huang and N. Wang, “Data-driven sparse structure selection for deep neural networks,” in *Proceedings of the European conference on computer vision (ECCV)*, 2018, pp. 304–320.

[19] P. Molchanov, S. Tyree, T. Karras, T. Aila, and J. Kautz, “Pruning convolutional neural networks for resource efficient inference,” in *International Conference on Learning Representations (ICLR)*, 2017, arXiv:1611.06440.

[20] R. Yu, A. Li, C.-F. Chen, J.-H. Lai, V. I. Morariu, X. Han, M. Gao, C.-Y. Lin, and L. S. Davis, “Nisp: Pruning networks using neuron importance score propagation,” in *Proceedings of the IEEE conference on computer vision and pattern recognition*, 2018, pp. 9194–9203.

[21] Z. Zhuang, M. Tan, B. Zhuang, J. Liu, J. Zhu *et al.*, “Discrimination-aware channel pruning for deep neural networks,” in *Advances in Neural Information Processing Systems (NeurIPS)*, 2018.

[22] Y. He, J. Lin, Z. Liu, H. Wang, L.-J. Li, and S. Han, “Amc: Automl for model compression and acceleration on mobile devices,” in *European Conference on Computer Vision (ECCV)*, 2018.

[23] T.-J. Yang, A. Howard, B. Chen, X. Zhang, A. Go, V. Sze *et al.*, “Netadapt: Platform-aware neural network adaptation for mobile applications,” in *European Conference on Computer Vision (ECCV)*, 2018.

[24] Z. Liu, J. Li, Z. Shen, G. Huang, S. Yan, and C. Zhang, “Metapruning: Meta learning for automatic neural network channel pruning,” in *IEEE International Conference on Computer Vision (ICCV)*, 2019.

[25] Y. He, G. Kang, X. Dong, Y. Fu, and Y. Yang, “Soft filter pruning for accelerating deep convolutional neural networks,” *arXiv preprint arXiv:1808.06866*, 2018.

[26] Y. He, P. Liu, Z. Wang, Z. Hu, and Y. Yang, “Filter pruning via geometric median for deep convolutional neural networks acceleration,” in *Proceedings of the IEEE/CVF conference on computer vision and pattern recognition*, 2019, pp. 4340–4349.

[27] M. Lin, R. Ji, Y. Wang, Y. Zhang, B. Zhang, Y. Tian, and L. Shao, “Hrank: Filter pruning using high-rank feature map,” in *Proceedings of the IEEE/CVF conference on computer vision and pattern recognition*, 2020, pp. 1529–1538.

[28] J.-H. Luo, J. Wu, and W. Lin, “Thinet: A filter level pruning method for deep neural network compression,” in *Proceedings of the IEEE international conference on computer vision*, 2017, pp. 5058–5066.

[29] Y. He, X. Zhang, and J. Sun, “Channel pruning for accelerating very deep neural networks,” in *Proceedings of the IEEE international conference on computer vision*, 2017, pp. 1389–1397.

[30] Y. Guo, A. Yao, and Y. Chen, “Dynamic network surgery for efficient dnns,” in *Advances in Neural Information Processing Systems (NeurIPS)*, 2016, arXiv:1608.04493.

[31] E. Denton, W. Zaremba, J. Bruna, Y. LeCun, and R. Fergus, “Exploiting linear structure within convolutional networks for efficient evaluation,” in *Advances in Neural Information Processing Systems (NeurIPS)*, 2014, arXiv:1404.0736.

[32] M. Jaderberg, A. Vedaldi, and A. Zisserman, “Speeding up convolutional neural networks with low rank expansions,” in *British Machine Vision Conference (BMVC)*, 2014.

[33] V. Lebedev, Y. Ganin, M. Rakhuba, I. Oseledets, and V. Lempitsky, “Speeding-up convolutional neural networks using fine-tuned cp-decomposition,” in *International Conference on Learning Representations (ICLR)*, 2015, arXiv:1412.6553.

[34] G. Hinton, O. Vinyals, and J. Dean, “Distilling the knowledge in a neural network,” *arXiv preprint arXiv:1503.02531*, 2015.

[35] A. Romero, N. Ballas, S. E. Kahou, A. Chassang, C. Gatta, and Y. Bengio, “Fitnets: Hints for thin deep nets,” in *International Conference on Learning Representations (ICLR)*, 2015.

[36] S. Zagoruyko and N. Komodakis, “Paying more attention to attention: Improving the performance of convolutional neural networks via attention transfer,” in *International Conference on Learning Representations (ICLR)*, 2017, arXiv:1612.03928.

[37] G. E. Hinton and R. R. Salakhutdinov, “Reducing the dimensionality of data with neural networks,” *Science*, vol. 313, no. 5786, pp. 504–507, 2006.

[38] P. Vincent, H. Larochelle, Y. Bengio, and P.-A. Manzagol, “Extracting and composing robust features with denoising autoencoders,” in *International Conference on Machine Learning (ICML)*, 2008.

[39] J. Bruna and S. Mallat, “Invariant scattering convolution networks,” in *IEEE Transactions on Pattern Analysis and Machine Intelligence*, 2013.

[40] O. Rippel, J. Snoek, and R. P. Adams, “Spectral representations for convolutional neural networks,” in *Advances in Neural Information Processing Systems (NeurIPS)*, 2015, arXiv:1506.03767.

[41] M. Mathieu, M. Henaff, and Y. LeCun, “Fast training of convolutional networks through ffts,” in *International Conference on Learning Representations (ICLR) Workshop*, 2014, arXiv:1312.5851.

[42] M. Tancik, P. P. Srinivasan, B. Mildenhall *et al.*, “Fourier features let networks learn high frequency functions in low dimensional domains,” in *Advances in Neural Information Processing Systems (NeurIPS)*, 2020, arXiv:2006.10739.

[43] V. Sitzmann, J. Martel, A. Bergman, D. Lindell, and G. Wetzstein, “Implicit neural representations with periodic activation functions,” in *Advances in Neural Information Processing Systems (NeurIPS)*, 2020, arXiv:2006.09661.

[44] C. Trabelsi, O. Bilaniuk, Y. Zhang *et al.*, “Deep complex networks,” in *International Conference on Learning Representations (ICLR)*, 2018, arXiv:1705.09792.

[45] M. Arjovsky, A. Shah, and Y. Bengio, “Unitary evolution recurrent neural networks,” in *International Conference on Machine Learning (ICML)*, 2016, arXiv:1511.06464.

[46] N. Tishby, F. C. Pereira, and W. Bialek, “The information bottleneck method,” *arXiv preprint arXiv:physics/0004057*, 2000.

[47] A. A. Alemi, I. Fischer, J. V. Dillon, and K. Murphy, “Deep variational information bottleneck,” in *International Conference on Learning Representations (ICLR)*, 2017, arXiv:1612.00410.

[48] S.-i. Amari, “Natural gradient works efficiently in learning,” *Neural Computation*, vol. 10, no. 2, pp. 251–276, 1998.

[49] J. Martens and R. Grosse, “Optimizing neural networks with kronecker-factored approximate curvature,” in *International Conference on Machine Learning (ICML)*, 2015, arXiv:1503.05671.

[50] M. Raghu, J. Gilmer, J. Yosinski, and J. Sohl-Dickstein, “Svcca: Singular vector canonical correlation analysis for deep learning dynamics and interpretability,” in *Advances in Neural Information Processing Systems (NeurIPS)*, 2017, arXiv:1706.05806.

[51] A. S. Morcos, M. Raghu, and S. Bengio, “Insights on representational similarity in neural networks with canonical correlation,” in *Advances in Neural Information Processing Systems (NeurIPS)*, 2018, arXiv:1806.05759.

[52] S. Kornblith, M. Norouzi, H. Lee, and G. Hinton, “Similarity of neural network representations revisited,” in *International Conference on Machine Learning (ICML)*, 2019, arXiv:1905.00414.

[53] A. Krizhevsky, “Learning multiple layers of features from tiny images,” University of Toronto, Tech. Rep., 2009.

[54] K. Simonyan and A. Zisserman, “Very deep convolutional networks for large-scale image recognition,” *arXiv preprint arXiv:1409.1556*, 2014.

[55] K. He, X. Zhang, S. Ren, and J. Sun, “Deep residual learning for image recognition,” in *Proceedings of the IEEE Conference on Computer Vision and Pattern Recognition (CVPR)*, 2016, pp. 770–778.

[56] G. Huang, Z. Liu, L. Van Der Maaten, and K. Q. Weinberger, “Densely connected convolutional networks,” in *Proceedings of the IEEE Conference on Computer Vision and Pattern Recognition (CVPR)*, 2017, pp. 4700–4708.

[57] S. Lin, R. Ji, C. Yan, B. Zhang, L. Cao, Q. Ye, F. Huang, and D. Doermann, “Towards optimal structured cnn pruning via generative adversarial learning,” in *Proceedings of the IEEE/CVF conference on computer vision and pattern recognition*, 2019, pp. 2790–2799.

[58] N. Otsu *et al.*, “A threshold selection method from gray-level histograms,” *Automatica*, vol. 11, no. 285-296, pp. 23–27, 1975.

[59] M. Shao, J. Dai, R. Wang, J. Kuang, and W. Zuo, “Cshe: network pruning by using cluster similarity and matrix eigenvalues,” *International Journal of Machine Learning and Cybernetics*, vol. 13, no. 2, pp. 371–382, 2022.

[60] Y. Chen and Z. Wang, “An effective information theoretic framework for channel pruning,” *arXiv preprint arXiv:2408.16772*, 2024.

- [61] G. Li, H. Shao, X. Deng, and Y. Jiang, “Adaptive convolutional network pruning through pixel-level cross-correlation and channel independence for enhanced model compression,” *Engineering Applications of Artificial Intelligence*, vol. 154, p. 110920, 2025.
- [62] G. Li, R. Li, T. Li, C. Shen, X. Zou, J. Wang, C. Wang, and N. Li, “Sfp: Similarity-based filter pruning for deep neural networks,” *Information Sciences*, vol. 689, p. 121418, 2025.
- [63] W. Wang, C. Fu, J. Guo, D. Cai, and X. He, “Cop: Customized deep model compression via regularized correlation-based filter-level pruning,” *arXiv preprint arXiv:1906.10337*, 2019.
- [64] J. Li, H. Shao, S. Zhai, Y. Jiang, and X. Deng, “A graphical approach for filter pruning by exploring the similarity relation between feature maps,” *Pattern Recognition Letters*, vol. 166, pp. 69–75, 2023.
- [65] Y. Sui, M. Yin, Y. Xie, H. Phan, S. Aliari Zonouz, and B. Yuan, “Chip: Channel independence-based pruning for compact neural networks,” *Advances in Neural Information Processing Systems*, vol. 34, pp. 24 604–24 616, 2021.
- [66] Y. Li, J. C. Van Gemert, T. Hoefer, B. Moons, E. Eleftheriou, and B.-E. Verhoeft, “Differentiable transportation pruning,” in *Proceedings of the IEEE/CVF International Conference on Computer Vision*, 2023, pp. 16 957–16 967.
- [67] G. Fang, X. Ma, M. Song, M. B. Mi, and X. Wang, “Depgraph: Towards any structural pruning,” in *Proceedings of the IEEE/CVF conference on computer vision and pattern recognition*, 2023, pp. 16 091–16 101.
- [68] B. Wang, C. Ma, B. Liu, N. Liu, and J. Zhu, “Filter pruning for cnn with enhanced linear representation redundancy,” *arXiv preprint arXiv:2310.06344*, 2023.
- [69] S. Elkerdawy, M. Elhoushi, H. Zhang, and N. Ray, “Fire together wire together: A dynamic pruning approach with self-supervised mask prediction,” in *Proceedings of the IEEE/CVF conference on computer vision and pattern recognition*, 2022, pp. 12 454–12 463.
- [70] J. Li, H. Shao, X. Deng, and Y. Jiang, “Efficient filter pruning: Reducing model complexity through redundancy graph decomposition,” *Neurocomputing*, vol. 599, p. 128108, 2024.
- [71] P. Wu, H. Huang, H. Sun, D. Liang, and N. Liu, “Cprnc: Channels pruning via reverse neuron crowding for model compression,” *Computer Vision and Image Understanding*, vol. 240, p. 103942, 2024.
- [72] Y. Chen, R. Zhou, B. Guo, Y. Shen, W. Wang, X. Wen, and X. Suo, “Discrete cosine transform for filter pruning,” *Applied Intelligence*, vol. 53, no. 3, pp. 3398–3414, 2023.

APPENDIX

VI. THEORETICAL RATIONALE

This section provides a formal rationale for why spectral reconstruction fidelity under a *low-capacity* autoencoder is a meaningful proxy for channel redundancy. Our goal is not to claim a universal guarantee of zero accuracy loss under pruning—which would be impossible without strong assumptions because pruning changes the model and thus the activation distribution—but to establish (i) a rigorous link between the proposed fidelity score and normalized reconstruction error, and (ii) conditions under which “high fidelity” implies that removing the corresponding channel is a *small* perturbation to the layer output in a well-defined norm.

A. Notation

Fix a layer ℓ and an output channel k . For a sample b , let $Z_{k,b} \in \mathbb{C}^{C_{\text{in}} \times H \times W}$ be the complex interaction field (Eq. (1)), and let $\widehat{Z}_{k,b}$ be its reconstruction obtained by spectral autoencoding and inverse FFT (Eq. (7)). Define the real-valued vectorization

$$\begin{aligned} v_{k,b} &= \text{vec}([\Re(Z_{k,b}), \Im(Z_{k,b})]) \in \mathbb{R}^D, \\ \hat{v}_{k,b} &= \text{vec}([\Re(\widehat{Z}_{k,b}), \Im(\widehat{Z}_{k,b})]) \in \mathbb{R}^D, \end{aligned}$$

where $D = 2C_{\text{in}}HW$. Let $u_{k,b} = v_{k,b}/\|v_{k,b}\|_2$ and $\hat{u}_{k,b} = \hat{v}_{k,b}/\|\hat{v}_{k,b}\|_2$ denote the unit-normalized vectors when norms are nonzero (in practice, an ε is used for numerical stability). The per-sample fidelity is

$$F_{k,b} = |\langle u_{k,b}, \hat{u}_{k,b} \rangle| \in [0, 1],$$

and the channel fidelity is the batch mean $\text{Fid}_k = \frac{1}{B} \sum_b F_{k,b}$ (Eq. (8)).

B. Fidelity is equivalent to normalized reconstruction error

We first formalize the exact relationship between fidelity and normalized ℓ_2 reconstruction error.

Proposition 1 (Fidelity–error identity). *For any nonzero vectors $v, \hat{v} \in \mathbb{R}^D$, let $u = v/\|v\|_2$ and $\hat{u} = \hat{v}/\|\hat{v}\|_2$. Define $F = |\langle u, \hat{u} \rangle|$. Then there exists a sign $s \in \{+1, -1\}$ such that*

$$\|u - s\hat{u}\|_2^2 = 2(1 - F). \quad (12)$$

Proof. Choose $s = \text{sign}(\langle u, \hat{u} \rangle)$, so that $\langle u, s\hat{u} \rangle = |\langle u, \hat{u} \rangle| = F$. Since $\|u\|_2 = \|\hat{u}\|_2 = 1$,

$$\|u - s\hat{u}\|_2^2 = \|u\|_2^2 + \|s\hat{u}\|_2^2 - 2\langle u, s\hat{u} \rangle = 2 - 2F = 2(1 - F).$$

□

a) *Interpretation.*: Proposition 1 shows that $1 - F$ is exactly the squared Euclidean distance between normalized descriptors up to a global sign. Therefore, high fidelity is not a heuristic: it is mathematically equivalent to small normalized reconstruction error of the interaction descriptor.

C. From descriptor reconstruction to output perturbation

Recall that, for sample b , we construct the interaction descriptor $Z_{k,b}^{(\ell)} \in \mathbb{C}^{C_{\text{in}} \times H \times W}$ by pairing the layer input with an *aligned* version of the channel output. Let $\mathcal{R} : \mathbb{R}^{H_1 \times W_1} \rightarrow \mathbb{R}^{H \times W}$ denote the (fixed) alignment operator used in Section III-B (bilinear resize when $H_1 \neq H$ or $W_1 \neq W$, and the identity otherwise), and define the aligned channel map

$$\bar{y}_{k,b} = \mathcal{R}(Y_{k,b}^{(\ell)}) \in \mathbb{R}^{H \times W}.$$

By construction of Eq. (1), the imaginary part of $Z_{k,b}^{(\ell)}$ is a broadcast of $\bar{y}_{k,b}$ across the input-channel axis:

$$\Im(Z_{k,b}^{(\ell)})_{c,:,:} = \bar{y}_{k,b} \quad \forall c \in \{1, \dots, C_{\text{in}}\}. \quad (13)$$

Hence $\bar{y}_{k,b}$ can be recovered from $Z_{k,b}^{(\ell)}$ by a *known linear operator*. Define $\mathcal{A} : \mathbb{C}^{C_{\text{in}} \times H \times W} \rightarrow \mathbb{R}^{H \times W}$ by

$$\mathcal{A}(Z) = \frac{1}{C_{\text{in}}} \sum_{c=1}^{C_{\text{in}}} \Im(Z)_{c,:,:}. \quad (14)$$

Then (13) implies $\mathcal{A}(Z_{k,b}^{(\ell)}) = \bar{y}_{k,b}$ and likewise $\mathcal{A}(\widehat{Z}_{k,b}^{(\ell)}) = \widehat{y}_{k,b}$.

Lemma VI.1 (Aligned channel extraction is stable). *For any $Z, \widehat{Z} \in \mathbb{C}^{C_{\text{in}} \times H \times W}$ with embeddings $v = \text{vec}([\Re(Z), \Im(Z)])$ and $\hat{v} = \text{vec}([\Re(\widehat{Z}), \Im(\widehat{Z})])$,*

$$\|\mathcal{A}(Z) - \mathcal{A}(\widehat{Z})\|_2 \leq \frac{1}{\sqrt{C_{\text{in}}}} \|v - \hat{v}\|_2. \quad (15)$$

Proof. Let $\Delta = \Im(Z) - \Im(\widehat{Z}) \in \mathbb{R}^{C_{\text{in}} \times H \times W}$. By definition, $\mathcal{A}(Z) - \mathcal{A}(\widehat{Z}) = \frac{1}{C_{\text{in}}} \sum_c \Delta_{c,:,:}$. Using Cauchy–Schwarz on the sum over c ,

$$\begin{aligned} \left\| \frac{1}{C_{\text{in}}} \sum_c \Delta_{c,:,:} \right\|_2 &\leq \frac{1}{C_{\text{in}}} \sum_c \|\Delta_{c,:,:}\|_2 \\ &\leq \frac{1}{\sqrt{C_{\text{in}}}} \left(\sum_c \|\Delta_{c,:,:}\|_2^2 \right)^{1/2} = \frac{1}{\sqrt{C_{\text{in}}}} \|\Delta\|_2. \end{aligned}$$

Finally, $\|\Delta\|_2 \leq \|v - \hat{v}\|_2$ because $v - \hat{v}$ contains both real and imaginary differences. □

Lemma VI.1 shows that accurately reconstructing the descriptor Z in ℓ_2 norm *necessarily* yields an accurate reconstruction of the aligned channel output $\bar{y} = \mathcal{R}(Y_k)$.

Lemma VI.2 (Non-normalized fidelity–error identity). *Let $v, \hat{v} \in \mathbb{R}^D$ be nonzero, $u = v/\|v\|_2$, $\hat{u} = \hat{v}/\|\hat{v}\|_2$, and $F = |\langle u, \hat{u} \rangle|$. Let $s = \text{sign}(\langle u, \hat{u} \rangle) \in \{\pm 1\}$. Then*

$$\|v - s\hat{v}\|_2^2 = (\|v\|_2 - \|\hat{v}\|_2)^2 + 2\|v\|_2\|\hat{v}\|_2(1 - F). \quad (16)$$

Proof. Expand: $\|v - s\hat{v}\|_2^2 = \|v\|_2^2 + \|\hat{v}\|_2^2 - 2s\langle v, \hat{v} \rangle$. Since $s\langle v, \hat{v} \rangle = \|v\|_2\|\hat{v}\|_2|\langle u, \hat{u} \rangle| = \|v\|_2\|\hat{v}\|_2 F$, we obtain $\|v - s\hat{v}\|_2^2 = \|v\|_2^2 + \|\hat{v}\|_2^2 - 2\|v\|_2\|\hat{v}\|_2 F = (\|v\|_2 - \|\hat{v}\|_2)^2 + 2\|v\|_2\|\hat{v}\|_2(1 - F)$. □

Theorem 1 (Fidelity bounds aligned channel perturbation). *Fix layer ℓ and channel k . For any sample b with nonzero $v_{k,b}$ and $\hat{v}_{k,b}$, let $F_{k,b} = |\langle u_{k,b}, \hat{u}_{k,b} \rangle|$ as in Section VI-B,*

and define $s = \text{sign}(\langle u_{k,b}, \hat{u}_{k,b} \rangle)$. Then the aligned channel perturbation satisfies

$$\frac{1}{\sqrt{C_{\text{in}}}} \sqrt{(\|v_{k,b}\|_2 - \|\hat{v}_{k,b}\|_2)^2 + 2\|v_{k,b}\|_2 \|\hat{v}_{k,b}\|_2 (1 - F_{k,b})} \leq \|\bar{y}_{k,b} - \hat{y}_{k,b}\|_2 \leq (17)$$

In particular, if $\|\hat{v}_{k,b}\|_2 \approx \|v_{k,b}\|_2$ and $F_{k,b} \geq 1 - \delta$, then $\|\bar{y}_{k,b} - \hat{y}_{k,b}\|_2 \lesssim \sqrt{\frac{2\delta}{C_{\text{in}}}} \|v_{k,b}\|_2$.

Proof. By Lemma VI.1, $\|\bar{y}_{k,b} - \hat{y}_{k,b}\|_2 \leq \frac{1}{\sqrt{C_{\text{in}}}} \|v_{k,b} - \hat{v}_{k,b}\|_2$. Choose the sign s as in Lemma VI.2; since $\|v - \hat{v}\|_2 \leq \|v - s\hat{v}\|_2$ for that choice of s , combine with (16) to obtain (17). \square

a) *Practical takeaway.*: Eq. (17) clarifies what fidelity can and cannot guarantee: high fidelity certifies that the aligned channel map embedded in the interaction descriptor is compressible under the chosen spectral reconstructor. However, fidelity alone is scale-invariant and can assign a high score to a large-magnitude but spectrally simple channel; this motivates the magnitude-aware fusion with the filter ℓ_1 norm in Section III-F and the minimum-keep safeguard in the implementation.

D. Why low capacity promotes redundancy discovery

The above results justify fidelity as a reconstruction metric; we now explain why using a *tiny* autoencoder is essential.

Let \mathcal{D}_ℓ be the distribution of spectral interaction descriptors $\tilde{F}_k^{(\ell)}$ induced by the data and the baseline network at layer ℓ . Training a reconstructor with a limited bottleneck dimension d can be viewed as learning an approximation to a low-dimensional set that captures the *most common* variability under \mathcal{D}_ℓ . In particular, if the interaction descriptors concentrate near a d -dimensional manifold \mathcal{M}_ℓ , then a reconstructor with effective dimension d can achieve low error on samples near \mathcal{M}_ℓ but must incur higher error on components orthogonal to it. Consequently, high fidelity identifies channels whose interaction descriptors remain close to the learned compressible structure, aligning with the pruning goal of removing channels that do not introduce unique directions.

We emphasize that this argument requires the autoencoder to be *capacity-limited*; a sufficiently powerful reconstructor could memorize training samples and yield uniformly high fidelity, destroying discriminability. Therefore, SCAP deliberately uses a tiny MLP reconstructor and a small activation pool for training, which empirically produces a meaningful spread of fidelity scores and robust pruning decisions.

E. Limits of the theory and practical safeguards

Theorem 1 provides a deterministic upper bound on the perturbation of the aligned channel map embedded in the interaction descriptor, in terms of cosine fidelity and descriptor magnitude mismatch. This bound concerns descriptor reconstruction quality; it is not an end-to-end accuracy guarantee after pruning. Pruning sets y_k to zero, changes activation distributions, and can affect subsequent nonlinear transformations.

Therefore, we use SCAP as a ranking criterion and adopt practical safeguards: (1) fuse fidelity with filter ℓ_1 magnitude to avoid pruning large-but-simple channels; (2) enforce a per-layer minimum-keep constraint; and (3) fine-tune the pruned model using a short schedule.

The descriptor uses an alignment operator \mathcal{R} when spatial sizes differ; the theory bounds perturbations in the aligned space $\bar{y} = \mathcal{R}(Y_k)$. For stride-1 convolutions, \mathcal{R} is the identity, so the bound applies directly to Y_k .

a) *Summary.*: Proposition 1 provides an exact identity between cosine fidelity and the normalized ℓ_2 reconstruction error of unit-norm descriptors. Leveraging the descriptor construction, Theorem 1 further shows that fidelity (together with descriptor magnitude mismatch) upper-bounds the perturbation of the aligned channel map embedded in the interaction descriptor. These results support using spectral reconstruction fidelity as a mathematically grounded compressibility signal for channel ranking, while practical pruning still relies on magnitude fusion and fine-tuning to control end-to-end performance.

VII. ADDITIONAL EXPERIMENTS

A. Ablation study ($\tau = 0.6$ on CIFAR-100)

a) *Ablation target and setting.*: As described in the main paper, our default SCAP importance is computed by **additive fusion** of the fidelity-derived term and a **set- ℓ_1** magnitude term (layer-wise normalized). Therefore, the correct ablation is to **remove the ℓ_1 term**, yielding a fidelity-only variant. In this appendix, we report the ablation under the **more aggressive threshold** $\tau = 0.6$ on CIFAR-100: **11-none** denotes *no* ℓ_1 magnitude (fidelity-only), while **SCAP** denotes the default additive fusion (fidelity + set- ℓ_1).

b) *Fine-tuning trajectories (Fig. 4).*: Figure 4 shows Top-1 accuracy curves during fine-tuning after pruning. Across backbones, both variants recover rapidly after the pruning point (around epoch ≈ 35), but their converged accuracies differ: (1) **VGG16**: SCAP consistently converges above 11-none (roughly $\sim 1\%$ absolute advantage at the end of training); (2) **ResNet56**: SCAP shows a similar advantage (about $\sim 1\%$ absolute); (3) **ResNet110**: 11-none slightly exceeds SCAP at convergence (about $\sim 1\%$ absolute), indicating that the magnitude term is not universally beneficial under very aggressive pruning on deeper residual networks; (4) **DenseNet40**: the two variants are nearly identical at convergence. Overall, under $\tau = 0.6$, adding set- ℓ_1 tends to *stabilize* pruning decisions and improve final accuracy on VGG16/ResNet56, while its effect can be neutral or slightly negative on ResNet110.

c) *Compression comparison (Fig. 5).*: Figure 5 reports the achieved compression (FR/PR) of the two ablation variants. Numerically:

- **VGG16**: FR 90.93% \rightarrow 90.70% and PR 92.52% \rightarrow 92.37% when moving from 11-none to SCAP.
- **ResNet56**: FR 82.54% \rightarrow 82.06% and PR 88.13% \rightarrow 87.12%.
- **ResNet110**: FR 84.34% \rightarrow 84.38% and PR 84.28% \rightarrow 84.36% (SCAP is slightly *more* compressive here).

- **DenseNet40:** FR 84.25% → 83.96% and PR 83.92% → 83.70%.

These values show that the two variants operate at *very similar compression levels* under $\tau = 0.6$ (differences are typically within $\sim 0.1\text{--}1.0\%$), so the observed accuracy gaps in Fig. 4 mainly reflect the **ranking/selection effect of including the set- ℓ_1 term**, rather than a large shift in compression strength.

d) Takeaway.: Under the aggressive regime $\tau = 0.6$, removing the ℓ_1 term (11-none) is a meaningful ablation because SCAP’s default importance *explicitly depends* on it. Empirically, the additive set- ℓ_1 term improves accuracy on VGG16/ResNet56 without materially changing FR/PR, while deeper residual architectures (ResNet110) can exhibit slight sensitivity where fidelity-only selection may be preferable. This supports our main design choice: **fidelity is the core redundancy signal, and set- ℓ_1 fusion is a practical safeguard**, but not a strict requirement in every backbone.

B. Exploratory experiments (fusion rules and operating-point selection)

a) Fusion rules and selection principle.: In Eq. (11), we evaluate three fusion rules to combine fidelity-based importance with the layer-normalized set- ℓ_1 magnitude term: (i) **additive fusion** (Add), (ii) **multiplicative fusion** (Mul), and (iii) **power-multiplicative fusion** (PowMul, weighted geometric mean). The key principle is that fusion should be selected by **jointly inspecting** (a) the **Top-1 accuracy recovery curves** and (b) the achieved **compression** (FR/PR), i.e., by choosing a desirable operating point on the accuracy-compression frontier.

b) Threshold $\tau = 0.5$ (Figs. 6–7).: At the milder threshold $\tau = 0.5$, Fig. 6 shows that Add and PowMul generally converge to similar (and higher) final accuracy, while Mul tends to converge lower. Meanwhile, Fig. 7 quantifies the compression differences:

- **VGG16:** Add achieves FR/PR 79.62/84.65, Mul increases to 90.72/94.13 (about +11.10 FR and +9.48 PR over Add), and PowMul yields 80.30/86.23 (intermediate PR gain with FR close to Add).
- **ResNet56:** Add 69.27/74.43, Mul 75.33/82.37 (about +6.06 FR and +7.94 PR), PowMul 68.74/75.53.
- **ResNet110:** Add 77.80/74.84, Mul 80.34/81.48 (about +2.54 FR and +6.64 PR), PowMul 74.04/72.66.
- **DenseNet40:** Add 74.77/73.66, Mul 77.79/83.20 (about +3.02 FR and +9.54 PR), PowMul 73.23/73.80.

Combining Fig. 6 and Fig. 7, Mul indeed provides higher compression, but its accuracy recovery is consistently weaker; Add is the most stable default, and PowMul often behaves as an intermediate option (slightly higher PR than Add with comparable accuracy trends).

c) Threshold $\tau = 0.6$ (Figs. 8–9).: Under the more aggressive threshold $\tau = 0.6$, the trade-off becomes sharper: Mul pushes compression further but tends to degrade accuracy recovery more noticeably (Fig. 8). Figure 9 quantifies the compression gains:

- **VGG16:** Add FR/PR 90.70/92.37, Mul increases to 95.85/96.97 (about +5.15 FR and +4.60 PR), PowMul 91.37/93.90.

- **ResNet56:** Add 82.06/87.12, Mul 85.53/91.23 (about +3.47 FR and +4.11 PR), PowMul 79.57/86.96.
- **ResNet110:** Add 84.38/84.36, Mul 86.92/90.10 (about +2.54 FR and +5.74 PR), PowMul 82.81/82.97.
- **DenseNet40:** Add 83.96/83.70, Mul 84.01/88.82 (FR nearly unchanged but PR improves by +5.12), PowMul 83.28/83.82.

Thus, at $\tau = 0.6$, Mul consistently yields the highest PR (and often higher FR), but Fig. 8 shows that it can lead to a larger accuracy gap during and after fine-tuning. Add remains the most reliable operating point, while PowMul can be chosen when one desires a modest PR increase with less risk than pure multiplication.

d) Overall recommendation.: Across thresholds, **Add** is the best default due to stable recovery and competitive FR/PR. **Mul** is preferable only when one explicitly prioritizes maximum compression and accepts a potentially larger accuracy drop. **PowMul** serves as an intermediate choice that can slightly increase PR while preserving much of Add’s stability. In summary, the selection should be made by jointly considering **Top-1 accuracy** and **FR/PR** on the curves in Figs. 6–9, i.e., by choosing the best Pareto operating point for the target deployment regime.

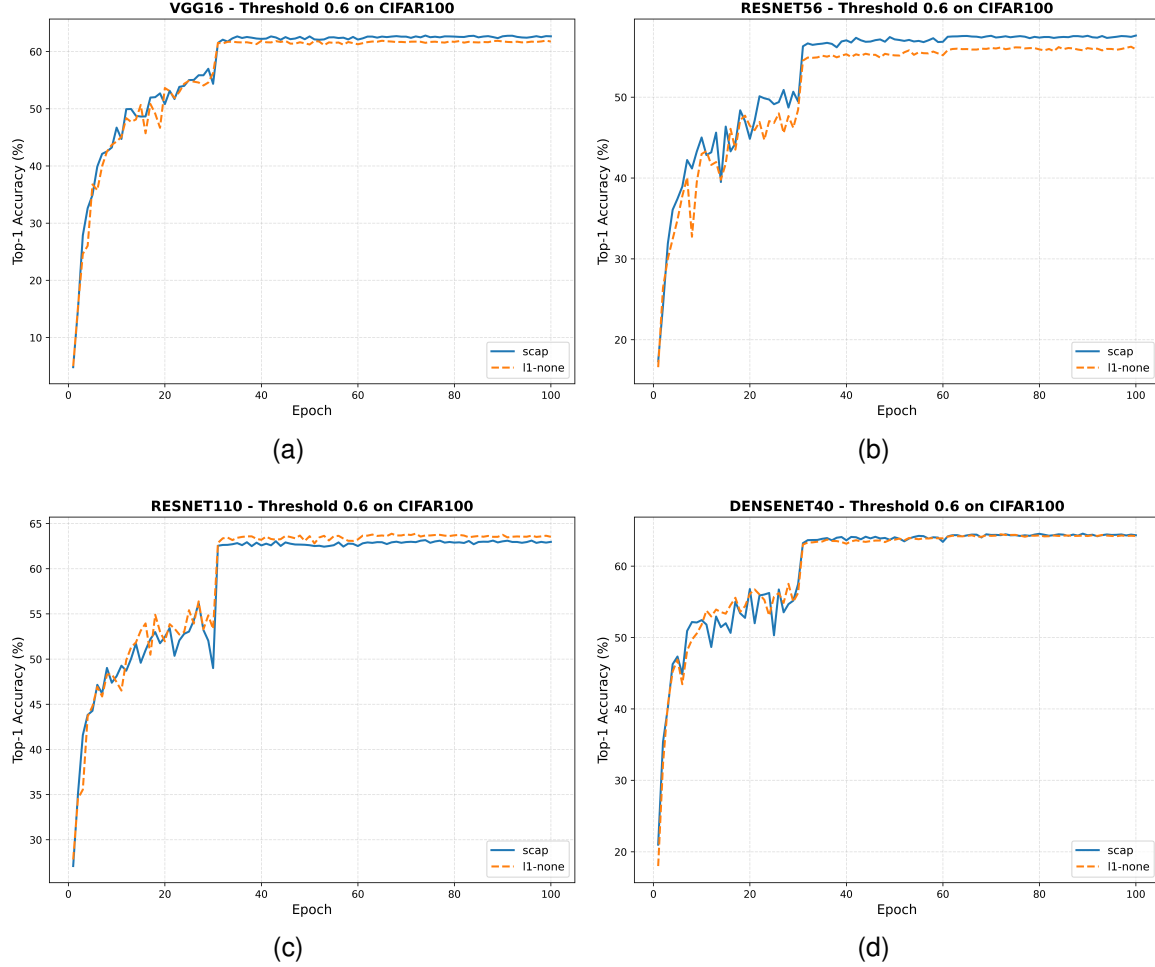


Fig. 4. Ablation at threshold $\tau = 0.6$ on CIFAR-100. **l1-none** denotes fidelity-only importance (removing the ℓ_1 magnitude term), while **SCAP** denotes the default additive fusion (fidelity + set- ℓ_1). We report Top-1 accuracy during fine-tuning for different backbones.

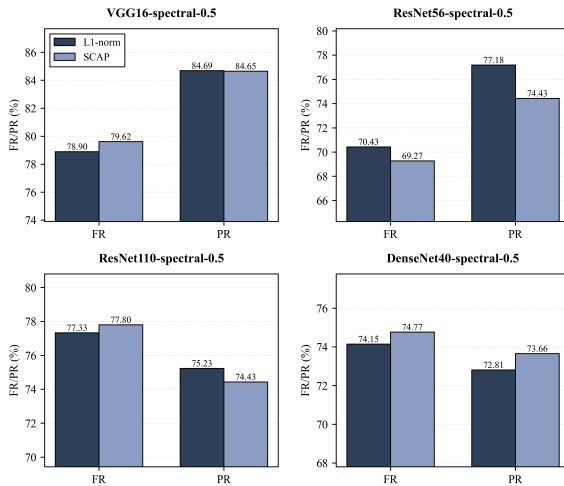


Fig. 5. Compression comparison (FR/PR) for the ablation at $\tau = 0.6$ on CIFAR-100. **l1-none** removes the ℓ_1 magnitude term; **SCAP** uses the default additive fusion (fidelity + set- ℓ_1).

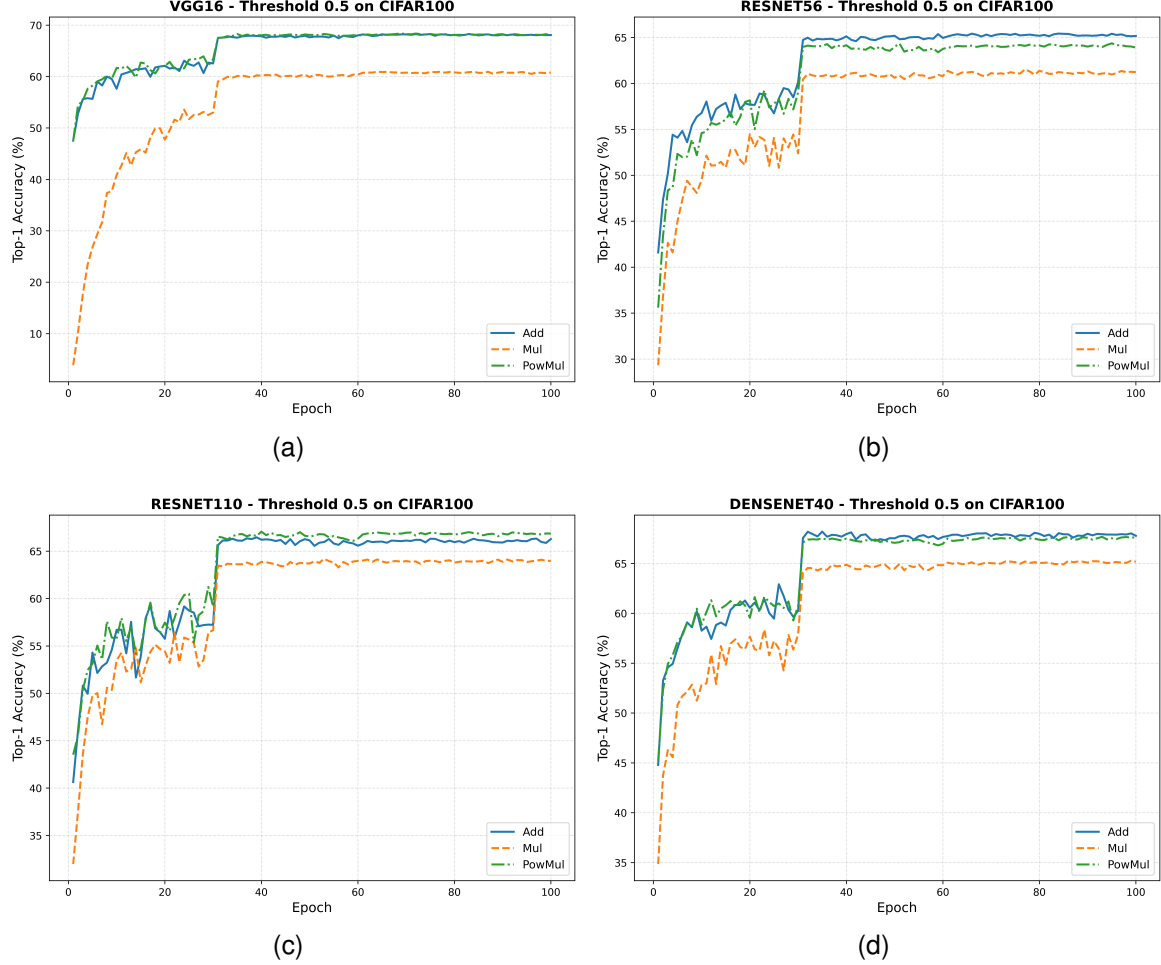


Fig. 6. Exploratory experiments at threshold $\tau = 0.5$ on CIFAR-100: Top-1 accuracy trajectories during fine-tuning under different fusion rules in Eq. (11) (Add / Mul / PowMul) across backbones.

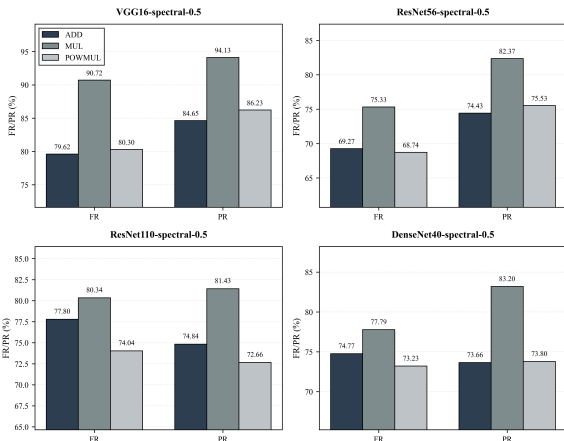


Fig. 7. Exploratory experiments at $\tau = 0.5$ on CIFAR-100: achieved compression (FR/PR) under Add / Mul / PowMul across backbones.

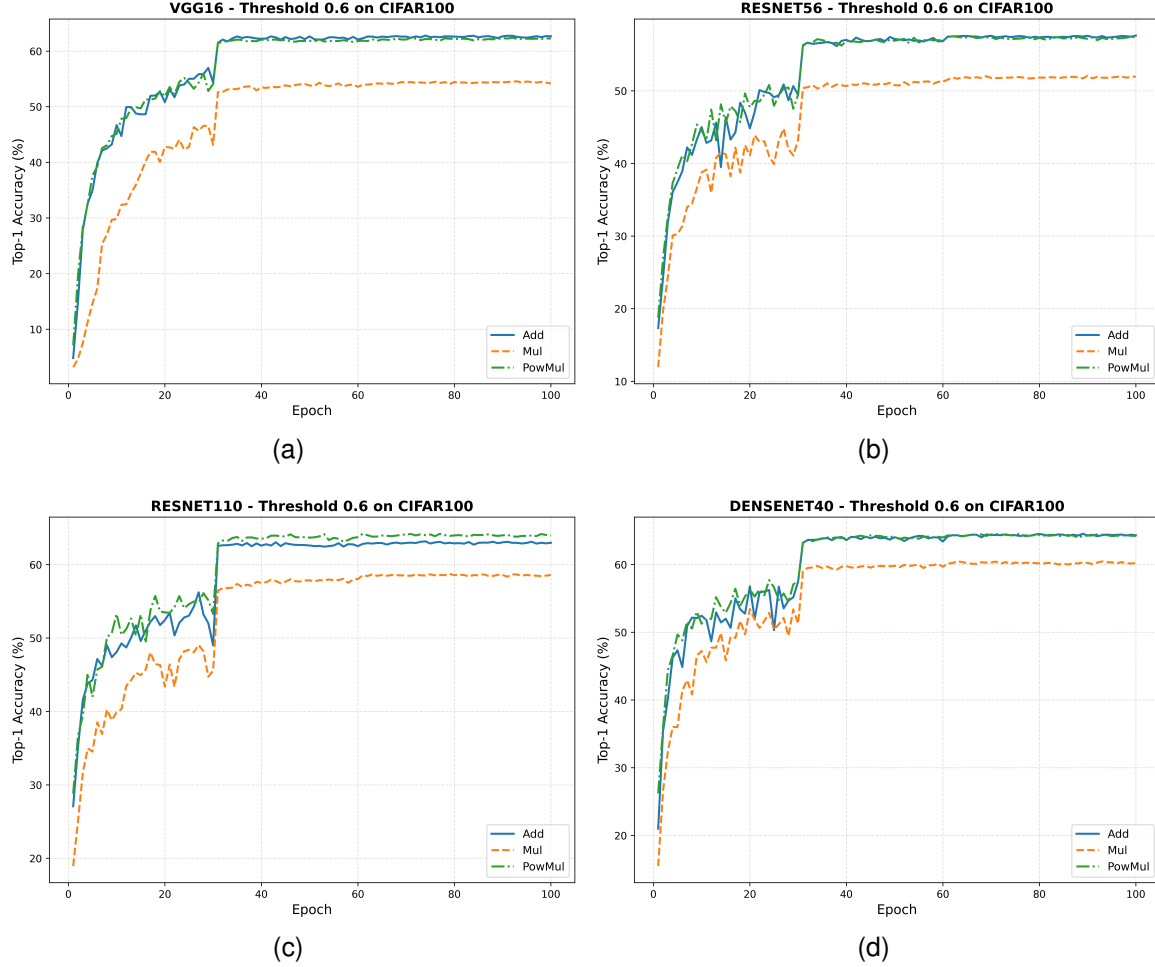


Fig. 8. Exploratory experiments at threshold $\tau = 0.6$ on CIFAR-100: Top-1 accuracy trajectories during fine-tuning under different fusion rules in Eq. (11) (Add / Mul / PowMul) across backbones.

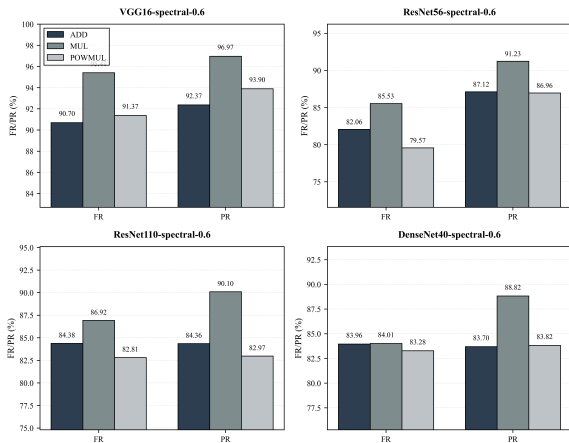


Fig. 9. Exploratory experiments at $\tau = 0.6$ on CIFAR-100: achieved compression (FR/PR) under Add / Mul / PowMul across backbones.